



## **A 1 km Hourly High-Resolution 3D Wind Field Dataset over the Yangtze River Delta Incorporating Dynamical Downscaling, Observational Assimilation, and Land Use Updates**

Zhengyan Zhang<sup>1,2</sup>, Yan-An Liu<sup>1,2\*</sup>, Xinjian Ma<sup>1,2</sup>, Zhenglong Li<sup>3</sup>, Pengbo Xu<sup>4</sup>, Juan Zhang<sup>5</sup>,  
Min Min<sup>6</sup>, Di Di<sup>7</sup>, Bo Li<sup>8</sup>, and Jun Li<sup>8</sup>

*1 Key Laboratory of Geographic Information Science (Ministry of Education), East China  
Normal University, Shanghai 200241, China;*

*2 School of Geographic Sciences, East China Normal University, Shanghai 200241, China;*

*3 Cooperative Institute for Meteorological Satellite Studies, University of Wisconsin-Madison,  
Madison, Wisconsin 53706, USA;*

*4 School of Mathematical Sciences, Key Laboratory of MEA (Ministry of Education), Shanghai  
Key Laboratory of PMMP, East China Normal University, Shanghai 200241, China;*

*5 Shanghai Zhangjiang Institute of Mathematics, Shanghai, China.*

*6 School of Atmospheric Sciences and Guangdong Province Key laboratory for Climate Change  
and Natural Disaster Studies, Sun Yat-sen University and Southern Laboratory of Ocean Science  
and Engineering, Zhuhai 519082, China;*

*7 Collaborative Innovation Center on Forecast and Evaluation of Meteorological Disasters,  
Nanjing University of Information Science and Technology, Nanjing 210044, China;*

*8 Innovation Center for FengYun Meteorological Satellite (FYSIC), National Satellite  
Meteorological Center (National Center for Space Weather), Beijing 100081, China.*

**Manuscript to be submitted to *Earth System Science Data***

**\*Corresponding author:** Yan-An Liu (yaliu@geo.ecnu.edu.cn)



## ABSTRACT

High-resolution three-dimensional (3D) wind field data are critical for a wide range of applications, including wind energy assessment, low-altitude aviation, air quality modeling, and extreme weather forecasting. Although ERA5 reanalysis remains widely used, its relatively coarse spatial resolution (~31 km) limits its ability to capture local-scale atmospheric processes. To address this, this study develops an hourly 3D dynamic wind field dataset with 1 km horizontal resolution covering the Yangtze River Delta (YRD) region during the summer months (June–August) from 2021 to 2023, namely YRD1km, generated through advanced dynamical downscaling of ERA5 using a customized Weather Research and Forecasting (WRF) model configuration. The methodology integrates multi-source observational nudging with high-resolution land use parameterization to enhance near-surface wind accuracy and terrain-induced flow representation, particularly in urban clusters and mountainous areas. Validation against ground-based observations confirms the superior performance of YRD1km over ERA5 for hourly 10-m wind components, with Mean Absolute Error (MAE) reduced by approximately 22% for U and 26% for V, Root Mean Square Error (RMSE) reduced by 18% for U and 23% for V, and Nash–Sutcliffe Efficiency (NSE) improved by 33% and 40%, respectively. On a daily mean basis, both MAE and RMSE are reduced to below 0.4 m/s, and NSE reaches approximately 0.88. Spatially, YRD1km captures finer spatial wind speed gradients and localized terrain-induced circulations that are not captured by ERA5. Temporally, consistent accuracy improvements with approximately 20% lower hourly error variability are seen when compared to ERA5. Vertically, 42.2% accuracy gains are observed in the near-surface layer when compared with radiosonde profiles. Moreover, in a representative convective storm case, YRD1km captures multi-level wind structures that are closely linked to the initiation and continuous development of deep convection, highlighting its



24 diagnostic advantage in high-impact weather events. Overall, the YRD1km 3D wind field dataset  
25 and its integrated methodological framework provide a robust foundation for regional  
26 meteorological applications, including high-resolution AI-based forecasting, renewable energy  
27 planning, and weather risk management in rapidly developing regions such as the YRD. The  
28 YRD1km 3D wind field dataset is available at <https://doi.org/10.57760/sciencedb.23752> (Zhang  
29 et al., 2025).

30 **Key words:** 3D wind field dataset; dynamical downscaling; multi-source observational  
31 nudging; high-resolution land use; Yangtze River Delta

32

## 33 1. Introduction

34 Accurate characterization of three-dimensional (3D) wind fields with high spatiotemporal  
35 resolution is fundamental to modern meteorological services, wind energy development, and the  
36 safe operation of low-altitude economy. Although widely used ERA5 atmospheric reanalysis  
37 datasets are capable of providing wind field variables that exhibit temporal continuity and physical  
38 consistency, their relatively coarse spatial resolution limits the capability to resolve regional-scale  
39 wind field features (Hu et al., 2023; Jung and Schindler, 2022), particularly in areas with complex  
40 terrain and intense urbanization (Molina et al., 2021).

41 The Yangtze River Delta (YRD), as one of the most intensely urbanized regions in China,  
42 exhibits evident spatiotemporal heterogeneity in local wind fields due to the combined effects of  
43 sea-land thermal contrasts, urban heat island effects, and boundary layer turbulence (Zhang et al.,  
44 2010). This presents significant challenges for precise wind energy resource assessment, urban  
45 ventilation capacity diagnosis, and early warning of wind storm events. To address these  
46 challenges, spatial downscaling of coarse-resolution reanalysis datasets has become a promising



47 strategy for improving regional wind field reanalysis and supporting fine-scale applications (Boé  
48 et al., 2007; Tang et al., 2016; Zhang et al., 2020).

49 Spatial downscaling techniques primarily include statistical downscaling and dynamical  
50 downscaling approaches. Statistical downscaling establishes statistical relationships between  
51 coarse-resolution meteorological variables and local observational data (Dayon et al., 2015;  
52 Tareghian and Rasmussen, 2013), enabling the acquisition of high-resolution wind field  
53 information at relatively low computational costs (Zamo et al., 2016). However, such methods  
54 often overlook the physical constraints among meteorological variables. In recent years, deep  
55 learning has been increasingly applied to enhance the accuracy of statistical downscaling of wind  
56 fields (Dujardin and Lehning, 2022; Dupuy et al., 2023; Höhlein et al., 2020; Lian et al., 2024; Liu  
57 et al., 2024a; Zhang and Li, 2021). Nevertheless, incorporating physical consistency into deep  
58 learning frameworks remains a significant challenge (Sun et al., 2024). In contrast, dynamical  
59 downscaling employs the fundamental equations governing the atmospheric dynamics to explicitly  
60 resolve physical processes, thereby reconstructing regional weather systems at high resolutions  
61 (Tang et al., 2016). Its effectiveness has been demonstrated in various applications (Bao et al.,  
62 2015; Liu et al., 2024b; Xu et al., 2021). Horvath et al. (2012) applied the Weather Research and  
63 Forecasting (WRF) model with sub-kilometer grid spacing over mountainous regions of Nevada  
64 and showed that dynamical downscaling significantly improved the representation of near-surface  
65 wind speed and variability compared to coarser reanalysis products. Notably, when combined with  
66 nudging techniques, the model's responsiveness to the actual atmospheric state is further enhanced  
67 (Harkey and Holloway, 2013; Lo et al., 2008).

68 Nudging, also known as Newtonian relaxation, is a data assimilation method that introduces  
69 forcing terms into numerical model equations to incrementally adjust model variables toward





70 observations or analysis fields (Hoke and Anthes, 1976). Compared with variational assimilation  
71 methods, nudging does not require the construction of an adjoint model or the estimation of  
72 background error covariance matrices. As a result, it offers a simpler implementation and lower  
73 computational cost (Daescu and Langland, 2013; Lei and Hacker, 2015). Research has  
74 demonstrated that this method has been successfully applied in the construction of several high-  
75 resolution reanalysis datasets. For example, the MERIDA HRES (4 km resolution, hourly) (Viterbo  
76 et al., 2024) and the BAYWRF (1.5 km resolution, daily) (Collier and Mölg, 2020) datasets both  
77 employ the WRF model to perform dynamical downscaling on ERA5 reanalysis data. By  
78 integrating nudging techniques, these datasets have reconstructed local wind field characteristics  
79 for Italy and the Bavarian region of Germany, respectively. Although dynamical downscaling  
80 demands substantial computational resources, advancements in regional model structures and  
81 high-performance computing technologies are expected to greatly improve its feasibility for  
82 regional complex terrain studies and non-climate research applications (Gutowski et al., 2020;  
83 Yuan et al., 2024).

84 Furthermore, accurate representation of land surface parameters is another critical factor  
85 influencing the performance of wind field dynamical downscaling. In recent years, high-resolution  
86 land use data have been increasingly incorporated into wind field modeling to optimize surface  
87 parameterization (De Bode et al., 2023; Fu et al., 2020; Santos-Alamillos et al., 2015). The updated  
88 land use datasets enable more precise characterization of various land surface features such as  
89 urban areas, mountainous regions, and water bodies, which improve simulation of terrain-induced  
90 flows and boundary layer processes, particularly in complex terrain regions (Golzio et al., 2021;  
91 Siewert and Kroszczynski, 2023).



In summary, this study presents the development of a 1-km hourly 3D dynamic wind field dataset over the YRD region (YRD1km), covering the period of the summer months (June to August) from 2021 to 2023. The YRD1km dataset is generated by applying a state-of-the-art dynamical downscaling technique to the ERA5 reanalysis data, integrating multi-source observational nudging, and updating land surface information with high-resolution ESA WorldCover 2020 (EWC2020) land use data. The resulting dataset provides enhanced accuracy in simulating near-surface winds and tropospheric dynamic structures, particularly in urban and mountainous areas where wind variability is often high.

This study evaluates the performance of YRD1km relative to ERA5, with a focus on both horizontal and vertical wind field accuracy. It also assesses the effectiveness of an integrated methodology that combines dynamical downscaling, observational nudging, and updated land use data in improving wind field simulations over regions with complex land surface characteristics and atmospheric variability. The findings highlight the potential of YRD1km to support a wide range of applications, such as localized weather forecasting, renewable energy planning, air quality modeling, and urban environmental management in rapidly urbanizing areas.

## **2. Data**

### **2.1 ERA5 Reanalysis Data**

The ERA5 reanalysis dataset (Hersbach et al., 2020), developed by the European Centre for Medium-Range Weather Forecasts (ECMWF), integrates global multi-source observations through 4D-Var data assimilation(<https://doi.org/10.24381/cds.bd0915c6>). It provides three-dimensional hourly atmospheric variables (e.g., temperature, humidity, wind fields, and pressure) with a horizontal resolution of  $0.25^{\circ} \times 0.25^{\circ}$  (about 31km), serving as a widely adopted benchmark in meteorological research. In this study, ERA5 supplies initial and boundary conditions for the



115 WRF model dynamical downscaling. Additionally, ERA5 serves as a baseline dataset for  
 116 comparative validation of YRD1km performance enhancements.

## 117 **2.2 Surface and Upper Air Weather Observations**

118 This study assimilates two observational datasets: (1) the NCEP ADP Global Upper Air and  
 119 Surface Weather Observations (<https://doi.org/10.5065/Z83F-N512>), comprising global terrestrial  
 120 stations, ocean buoys, ships, radiosondes, aircraft reports, and ASCAT satellite-derived winds from  
 121 the Global Telecommunication System (GTS), and (2) hourly data from Automatic Weather  
 122 Stations (AWS) operated by the China Meteorological Administration (CMA) (<http://data.cma.cn/>).  
 123 The spatial distributions of the two observational datasets over the YRD are illustrated in Figure  
 124 1a. The NCEP ADP dataset provides three-dimensional conventional meteorological  
 125 measurements from multiple observational platforms. As a complement to the NCEP ADP dataset,  
 126 the CMA AWS network delivers high-density surface observations across China, with a total of  
 127 2,169 stations—approximately six times the number of surface stations available from the NCEP  
 128 ADP dataset within the Chinese domain. This higher station density significantly enhances the  
 129 spatial representativeness of near-surface meteorological conditions in the YRD region. Using  
 130 Observation Nudging assimilation techniques, these datasets collectively correct systemic biases  
 131 in ERA5's near-surface fields within the WRF framework, enhancing the model's capacity to  
 132 resolve localized circulation patterns. The AWS data further act as a cross-validation source to  
 133 quantify YRD1km's accuracy improvements.

## 134 **2.3 High-resolution Land Cover Geographical Data**

135 Conventional land use datasets in WRF (USGS 1992-1993 or MODIS 2001) (Anderson et  
 136 al., 1976) are limited in their ability to reflect the rapid urban expansion and evolving land surface  
 137 characteristics of the YRD region. To address this, we integrate the EWC2020 dataset—a global



land cover product with 10-meter spatial resolution that classifies 11 surface types (e.g., built-up areas, croplands, water bodies) (<https://esa-worldcover.org/en>). By updating WRF's land surface parameters with EWC2020, we refine the representation of aerodynamic roughness lengths and urban heat island effects. For instance, reclassifying Shanghai's Pudong district from Moderate Resolution Imaging Spectroradiometer (MODIS) "mixed urban" to EWC2020 "high-intensity built-up" improves wind field simulations by better capturing drag effects from high-rise structures, as validated against AWS observations.

### 3. Methods

#### 3.1 WRF Model Configuration for Dynamical Downscaling

This study employs the WRF-ARW model (v4.4.2) (Skamarock et al., 2019) to establish a dynamic downscaling framework, enhancing the spatial resolution of ERA5 reanalysis data from ~31 km to 1 km. The model domain is configured with a triple-nested grid centered at (29.36°N, 115.65°E) with horizontal resolutions of 9 km (D01, with 342×305 grid points), 3 km (D02, with 529×640 grid points), and 1 km (D03, with 919×949 grid points). The innermost domain, D03, covers the entire YRD region (Figure 1a) and is designed to capture local circulation features associated with urban clusters, lakes, and hilly terrain at a kilometer-scale resolution. In the vertical direction, 61 terrain-following eta levels are used, with the model top set at 10 hPa, which facilitates a detailed resolution of boundary layer dynamics. Through sensitivity testing, the following physical parameterization schemes were selected: the Thompson microphysics scheme (Thompson et al., 2008), which is well-suited for high-resolution cloud microphysics; the Dudhia shortwave radiation (Dudhia, 1989) and RRTM longwave radiation schemes (Mlawer et al., 1997) for radiative transfer; and for boundary layer and land surface processes, the YSU non-local closure scheme (Hong et al., 2006) coupled with the Noah land surface model (Tewari et al., 2004), which



enhances the representation of near-surface turbulent exchanges. The Kain-Fritsch cumulus parameterization scheme (Kain, 2004) is applied only in the outer grid (D01) to mitigate uncertainties in the “gray zone” below the 3 km grid resolution.

To reduce the accumulation of model errors, a cold-start strategy is implemented, with simulations initiated four times daily at 00, 06, 12, and 18 UTC, respectively. Each run generates a continuous 6-hour forecast period, from which the first hour is discarded as model spin-up. Ultimately, this approach produces a continuous hourly three-dimensional wind field dataset.

### 3.2 Conventional Observational Data Assimilation via Nudging

While WRF dynamical downscaling enhances dataset resolution and preserves dynamical constraints and physical consistency, it struggles to capture fine-scale wind field features over complex underlying surfaces (e.g., urban clusters, water bodies) without dense observational constraints. To address this, this study employs the Four-Dimensional Data Assimilation (FDDA) technique, integrating conventional observations and ERA5 reanalysis fields through a Nudging approach, thereby balancing localized dynamical processes and large-scale circulation consistency. The core formulation of this approach is:

$$\frac{\partial x}{\partial t} = F(x) + G \cdot W(t) \cdot (x_{obs} - x) \quad (1)$$

where  $x$  represents the model variable,  $F(x)$  denotes the model dynamical equations,  $G$  is the relaxation coefficient, and  $W(t)$  is the temporal weighting function.

This study adopts a hybrid Nudging scheme combining two strategies: (1) Observation Nudging (ON): Direct assimilation of in situ observations from CMA AWS and NCEP ADP to dynamically refine local wind fields. (2) Analysis Nudging (AN): Application of ERA5 reanalysis fields as constraints to impose large-scale adjustments across the entire model domain hourly (Stauffer and Seaman, 1990), preventing deviations from large-scale circulation patterns. Thus, the



combined ON+AN assimilation scheme ensures both large-scale consistency and enhanced regional meteorological representation.

Taking the nudging experiment on June 1, 2022, as an example, the study quantitatively evaluates wind field accuracy over the YRD against ground-based observations using three statistical metrics: Mean Absolute Error (MAE), Root Mean Square Error (RMSE), and the Nash-Sutcliffe Efficiency coefficient (NSE; Nash and Sutcliffe, 1970), defined as follows:

$$MAE = \frac{1}{n} \sum_{i=1}^n |A_i - O_i| \quad (2)$$

$$RMSE = \sqrt{\frac{1}{n} \sum_{i=1}^n (A_i - O_i)^2} \quad (3)$$

$$NSE = 1 - \frac{\sum_{i=1}^n (A_i - O_i)^2}{\sum_{i=1}^n (O_i - \bar{O})^2} \quad (4)$$

where  $A_i$  represents simulated values from either ERA5 reanalysis or the dynamically downscaled results,  $O_i$  denotes corresponding in situ observations,  $n$  is the total number of spatiotemporally matched observation–simulation pairs. The NSE metric ranges from  $-\infty$  to 1, with values approaching 1 indicating perfect agreement between simulations and observations. As shown in Table 1, compared to ERA5 data, the ON+AN assimilated dataset demonstrates significant improvements across all statistical metrics for both the 10-m zonal (U10m) and meridional (V10m) wind components. In particular, the MAE is reduced by 26% for U10m and 27% for V10m, the RMSE is reduced by 22% for U10m and 24% for V10m, and the NSE is enhanced by 39% for U10m and 42% for V10m. These results confirm that the ON+AN hybrid assimilation scheme substantially enhances the precision of high-resolution wind field datasets in the YRD region.

*Table 1. Comparison of surface (10-m) wind field performance between the ON+AN experiment and ERA5 reanalysis over the YRD region.*

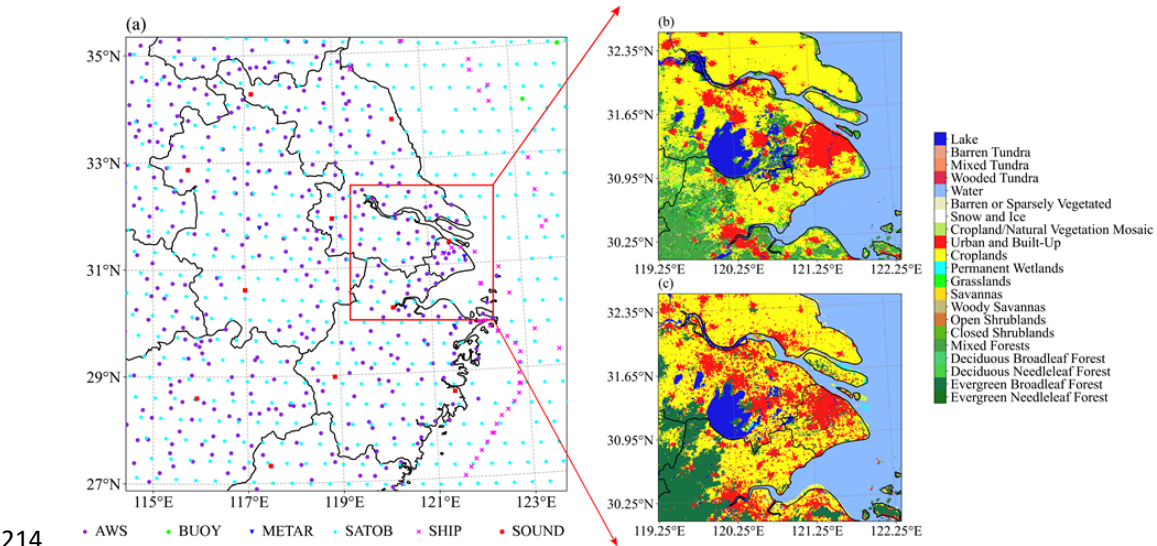
| Variable | Sample size | MAE (m/s) | RMSE (m/s) | NSE |
|----------|-------------|-----------|------------|-----|
|----------|-------------|-----------|------------|-----|



|      |      | ERA5  | ON+AN        | ERA5  | ON+AN        | ERA5  | ON+AN        |
|------|------|-------|--------------|-------|--------------|-------|--------------|
| U10m | 8107 | 1.203 | <b>0.894</b> | 1.583 | <b>1.239</b> | 0.343 | <b>0.597</b> |
| V10m | 8107 | 1.287 | <b>0.940</b> | 1.692 | <b>1.289</b> | 0.236 | <b>0.556</b> |

205 **3.3 Impact of High-Resolution Land Use Data Updates**

206 To address the impacts of rapid urbanization on wind field simulations in the YRD, this study  
207 enhances land surface characterization by updating the default MODIS 2001 land use data in the  
208 WRF model with the EWC2020 dataset at 10-meter resolution. Comparative analysis reveals  
209 substantial discrepancies between MODIS 2001 and EWC2020, particularly in Shanghai's  
210 metropolitan core (Figure 1b and 1c). The EWC2020 dataset resolves critical urban morphological  
211 features, including urban sprawl boundaries, park green spaces within city centers, and modified  
212 water-cropland interfaces, thereby more accurately capturing spatial heterogeneity in surface  
213 properties.



214 *Figure 1. Spatial distributions of key datasets used in this study. (a) Coverage of the innermost*  
215 *WRF domain (D03, 1-km resolution) over the YRD, along with the distribution of CMA Automatic*  
216 *Weather Stations (AWS) and the spatial coverage of NCEP ADP multi-source conventional*  
217 *Weather Stations (AWS) and the spatial coverage of NCEP ADP multi-source conventional*



218 observations used for nudging assimilation. The red box shows the region to highlight (b) Land  
219 use classification from the default MODIS 2001 dataset in WRF and (c) Updated high-resolution  
220 land use classification based on the EWC2020 product.

221 To quantify land use update effects on wind field simulations, we conduct two experiments  
222 under the ON+AN assimilation framework: 1) LU-MODIS: Retains default MODIS-based land  
223 use types; 2) LU-ESA2020: Incorporates the refined ESA2020-derived surface parameters. Using  
224 the June 1, 2022 case study, validation metrics (Table 2) demonstrate small but obvious positive  
225 impacts across all metrics for the LU-ESA2020 experiment compared to LU-MODIS. These  
226 results confirm the value of high-resolution land use updates in resolving urbanization-induced  
227 land-atmosphere interactions.

228 *Table 2. Statistical evaluation of land use sensitivity experiments conducted over the YRD region.*

| Variable | Sample size | MAE (m/s) |              | RMSE (m/s) |              | NSE       |              |
|----------|-------------|-----------|--------------|------------|--------------|-----------|--------------|
|          |             | LUT-MODIS | LUT-ESA2020  | LUT-MODIS  | LUT-ESA2020  | LUT-MODIS | LUT-ESA2020  |
| U10m     | 8107        | 0.894     | <b>0.886</b> | 1.239      | <b>1.232</b> | 0.597     | <b>0.602</b> |
| V10m     | 8107        | 0.940     | <b>0.933</b> | 1.289      | <b>1.282</b> | 0.556     | <b>0.561</b> |

229 **3.4 High-Resolution 3D Wind Field Dataset Generation**

230 Building on the evaluation results in section 3.2 and 3.3, this study develops a systematic  
231 framework for generating the YRD1km dataset over the YRD region, as shown in Figure 2. In the  
232 preprocessing stage, observational constraints for nudging were derived from the integration and  
233 quality control (QC) of NCEP ADP and CMA AWS datasets. Surface parameterization was refined  
234 by replacing the default MODIS 2001 land-use data with the updated ESA 2020 dataset. For model  
235 simulation, ERA5 reanalysis provided the initial and boundary conditions for a triple-nested WRF  
236 configuration (9 km → 3 km → 1 km). The updated surface parameters were used to optimize the  
237 static fields, while a suite of optimized physical schemes and a cold-start initialization strategy  
238 were applied to suppress error accumulation. A hybrid observational nudging scheme (ON + AN)





239 was employed to enhance the model's consistency with observed atmospheric states, resulting in  
240 continuous hourly 3D wind vector outputs at 1-km horizontal resolution and 61 vertical levels  
241 during the summer months (June – August) from 2021 to 2023.

242 Comprehensive multi-dimensional validation was conducted using both surface station  
243 observations and radiosonde profiles. The near-surface wind performance was evaluated through  
244 MAE, RMSE, and NSE metrics, capturing the overall, spatial, and temporal accuracy of the dataset.  
245 In addition, radiosonde-derived wind profiles were used to assess the vertical structure of the  
246 reconstructed fields. A dedicated case study further demonstrates the capability of YRD1km to  
247 resolve fine-scale dynamical features, confirming its superior performance compared to ERA5 and  
248 highlighting the effectiveness of the integrated approach in high-resolution wind field  
249 reconstruction.

250 Comprehensive multi-dimensional validation was performed using both surface station  
251 observations and radiosonde profiles. The near-surface wind simulation performance was assessed  
252 through MAE, RMSE, and NSE metrics, to evaluate the overall, spatial, and temporal accuracy of  
253 the dataset. In addition, radiosonde-derived vertical wind profiles were used to examine the fidelity  
254 of the reconstructed wind field structure in the lower and middle troposphere. Furthermore, a  
255 typical case study highlights the capability of the YRD1km dataset to capture fine-scale dynamical  
256 features, demonstrating clear improvements over ERA5 and underscoring the effectiveness of the  
257 integrated approach in high-resolution wind field reconstruction.

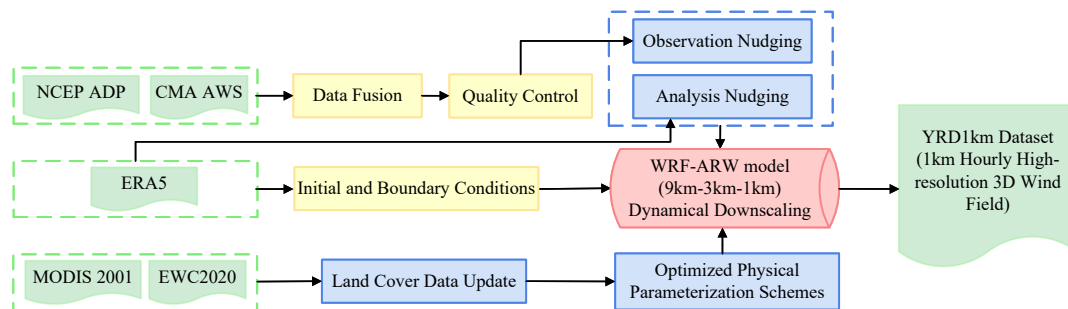


Figure 2. The schematic workflow of YRD1km 3D wind field generation.

## 4. Results and Discussion

### 4.1 Evaluation of YRD1km High-Resolution Dataset Accuracy

#### 4.1.1 Accuracy Evaluation of YRD1km and ERA5 Based on AWS Observations

The study conducted a comprehensive evaluation of the near-surface wind field accuracy using YRD AWS observational data on June 1, 2022. Due to the different spatial resolutions of YRD1km and ERA5, a nearest-grid-point matching method was adopted for comparison with station observations (Liu et al., 2025). As shown in Figure 3, scatterplots of the 10-m wind field U and V components for both ERA5 and YRD1km datasets were analyzed to assess their respective simulation capabilities. Overall, YRD1km exhibited superior performance in both U and V components, as evidenced by higher NSE coefficients, lower MAE and RMSE, and a tighter scatter distribution. Regression slopes for YRD1km were also notably closer to the 1:1 reference line, indicating a more accurate representation of the near-surface wind field compared to ERA5. For the U component (Figure 3a, c), ERA5 presented an NSE of 0.34, with MAE and RMSE of 1.20 m/s and 1.58 m/s, respectively, and a regression slope of only 0.42, with increasing deviations under higher wind speed conditions. In contrast, YRD1km achieved a significant improvement with an NSE of 0.60, MAE reduced to 0.89 m/s, RMSE reduced to 1.23 m/s, and an increased regression slope of 0.64, significantly reducing systematic biases. Further analysis based on the



sign of the U component revealed that ERA5 exhibited a consistent underestimation of both  
 easterly winds ( $U < 0$ ) and westerly winds ( $U > 0$ ), particularly under stronger wind conditions ( $|U| > 2$   
 m/s). This finding aligns with previous reports by Hu et al. (2023). While YRD1km also exhibited  
 a similar underestimation pattern, its magnitude was notably reduced, indicating an improved  
 representation of directional wind components compared to ERA5. Additionally, as wind speed  
 increased, scatter dispersion became more pronounced, with fewer samples in the high wind speed  
 range, adding challenges to accurate simulation.

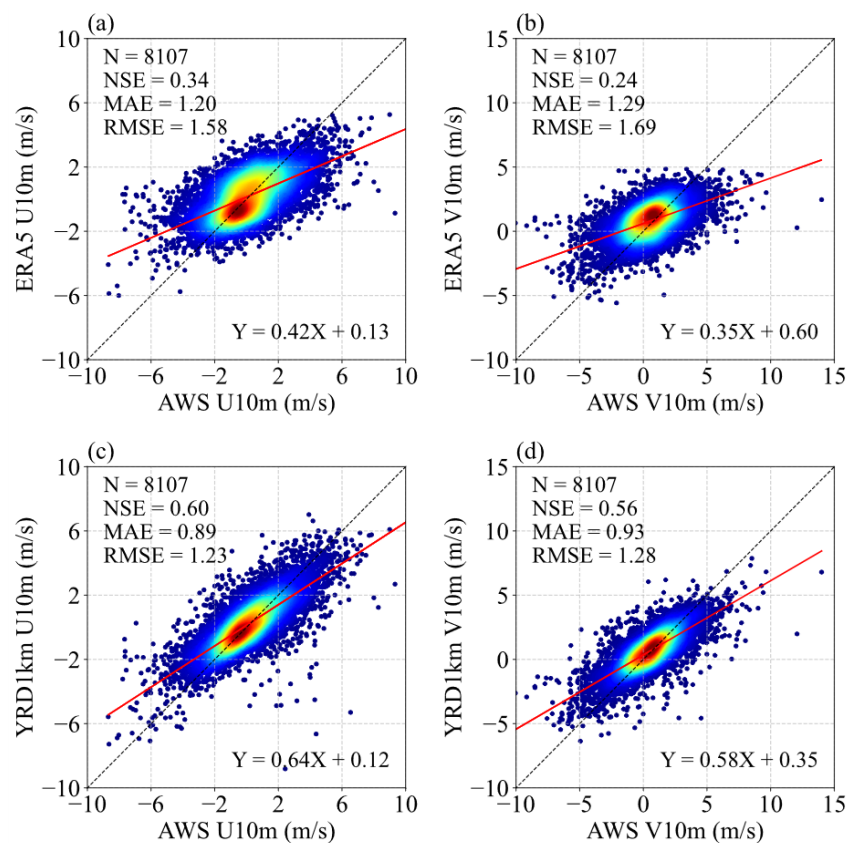


Figure 3. Scatterplot evaluation of 10-m wind components over the YRD region: (a) ERA5  
 U10m, (b) ERA5 V10m, (c) YRD1km U10m, and (d) YRD1km V10m.



For the V component (Figure 3b, d), ERA5 showed an even lower NSE of 0.24, with MAE and RMSE of 1.29 m/s and 1.69 m/s, respectively, and a regression slope of 0.35, indicating a less accurate simulation. Conversely, YRD1km significantly improved the NSE to 0.56, reduced MAE to 0.93 m/s, RMSE to 1.28 m/s, and increased the regression slope to 0.58. Similar to the U component, the V component displayed a directional-dependent error pattern, with an underestimation of both northerly winds ( $V < 0$ ) and southerly winds ( $V > 0$ ), especially under stronger wind conditions. The increasing scatter dispersion and simulation uncertainty with higher wind speeds further highlight the challenges and needs of reproducing complex wind fields.

Results in Figure 3 are based on hourly data. Considering that climate research emphasizes the use of daily data to smooth short-term fluctuations and reveal long-term trends (Kotlarski et al., 2019; Nashwan et al., 2019; Zhang et al., 2024), this study further examined the simulation accuracy of 10-m wind field at the daily mean scale. The comparison results based on daily mean observations from 332 AWS stations in the YRD region (Table 3) demonstrate that YRD1km maintains a stable accuracy advantage over ERA5 across all evaluated metrics for the U and V components, as well as wind speed at 10-m height. Notably, the daily mean values of the U and V components exhibited better statistical performance than their hourly counterparts, as temporal averaging effectively mitigates short-term fluctuations and random errors, enhancing simulation stability. Additionally, compared to 10-m wind speed (WSPD10m), the U and V components demonstrated greater improvements in error metrics, with NSE values closer to 1. This is primarily because wind speed is a scalar variable, while U and V components are vectors accounting for wind direction errors. The scale-dependent improvements emphasize the application value of YRD1km for both short-term weather monitoring and long-term climate analyses in the YRD region.



To further assess the robustness of the YRD1km dataset, an independent validation was performed by randomly withholding a subset of AWS station data from the nudging process. Despite the exclusion of these stations from direct observational nudging, YRD1km still outperforms ERA5 in terms of wind field accuracy at these independent locations (figure not shown). This result suggests that improving the representation of small-scale surface parameters may require a denser surface observation network to support more localized data assimilation.

*Table 3. Statistical comparison of daily 10-m wind fields between ERA5 and YRD1km datasets over the YRD region.*

| Variable | Indicator  | Data   |        | Improvement  |
|----------|------------|--------|--------|--------------|
|          |            | ERA5   | YRD1km | (%)          |
| U10m     | MAE (m/s)  | 0.543  | 0.289  | <b>46.67</b> |
|          | RMSE (m/s) | 0.687  | 0.370  | <b>46.04</b> |
|          | NSE        | 0.608  | 0.886  | <b>70.09</b> |
| V10m     | MAE (m/s)  | 0.575  | 0.311  | <b>45.96</b> |
|          | RMSE (m/s) | 0.750  | 0.398  | <b>46.84</b> |
|          | NSE        | 0.556  | 0.875  | <b>71.85</b> |
| WSPD10m  | MAE (m/s)  | 0.622  | 0.479  | <b>22.98</b> |
|          | RMSE (m/s) | 0.814  | 0.605  | <b>25.70</b> |
|          | NSE        | -0.185 | 0.346  | <b>44.81</b> |

#### 4.1.2 Comparison of spatial variations between YRD1km and ERA5

Building upon the preceding quantitative accuracy assessment, the study further examines the spatial variations of near-surface wind fields represented by the YRD1km and ERA5 datasets, as illustrated in Figure 4. Overall, while both datasets (Figure 4a and 4c) adequately capture the large-scale spatial variations of 10-m wind speeds across the YRD, YRD1km demonstrates a notable advantage in resolving mesoscale and local-scale wind field characteristics. Specifically,



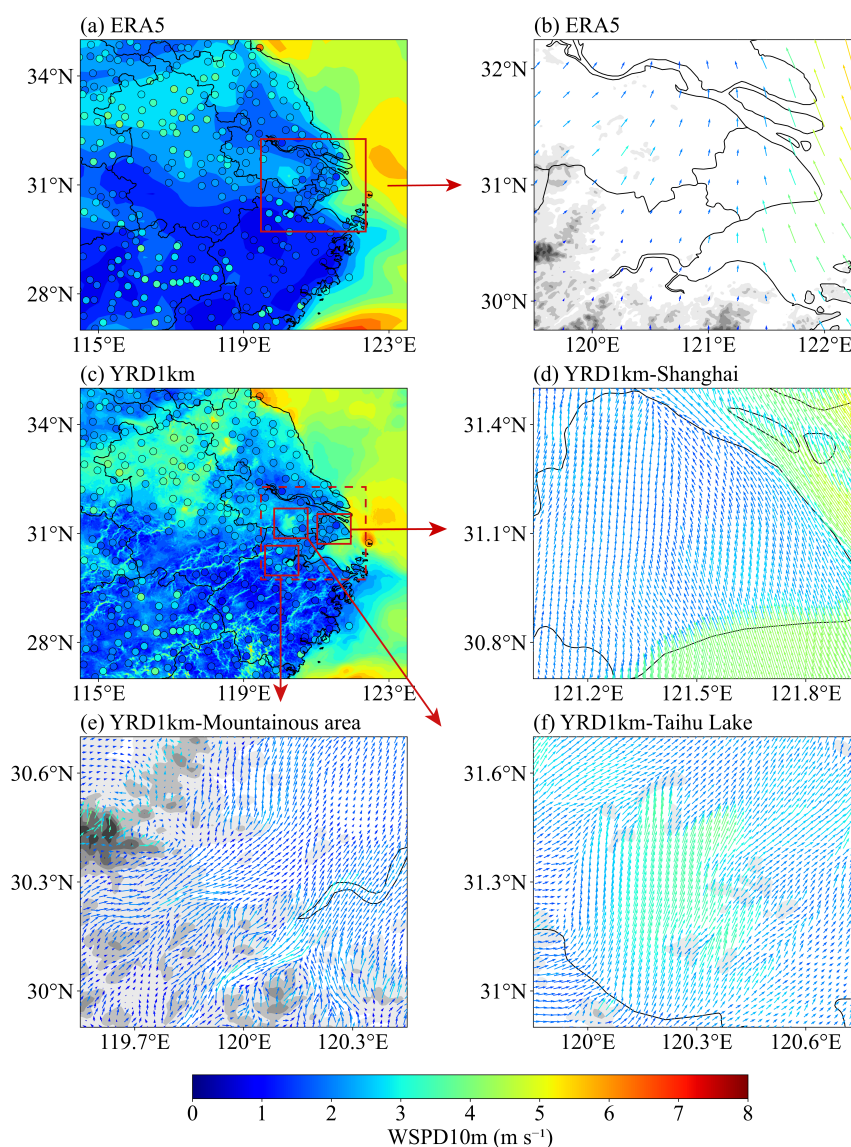
YRD1km (Figure 4c) offers a much finer spatial representation of wind speed variations compared to ERA5, closely aligned with observational data, particularly over complex terrain and urbanized areas. This includes enhanced wind speed zones over large water bodies such as Lake Taihu, realistic gradients in mountainous regions like southern Anhui and Zhejiang driven by valley flows and orographic effects, as well as improved wind speed structures over highly urbanized areas such as Shanghai. Furthermore, ERA5 exhibits underestimation of wind speed maxima near offshore observation points (e.g., in the East China Sea). YRD1km mitigates these biases through assimilation of AWS data via a nudging approach, enabling better alignment with ground truth observations and significantly enhancing the fidelity of simulated wind fields.

These spatial advantages are further highlighted through detailed analyses of wind vector fields. As shown in Figure 4b, ERA5 exhibits an overly smoothed wind field with limited flow differentiation near topographic boundaries. In contrast, the YRD1km dataset presents highly structured and terrain-conforming wind directions. Over the Shanghai metropolitan area (Figure 4d), the wind field aligns with urban morphological structures, showing clear directional deflection near city boundaries and dense river network regions, primarily due to thermal forcing and surface drag associated with urbanization. In the mountainous region near Hangzhou (Figure 4e), the wind field captures pronounced curvature and flow separation that closely follow terrain contours, effectively representing multiple terrain-induced processes such as valley and slope winds. Over Lake Taihu (Figure 4f), YRD1km simulates a divergent wind pattern, with significantly higher wind speeds over the lake surface relative to surrounding land, indicative of thermally driven lake–land breeze circulations.

Collectively, the spatial patterns observed in both scalar (wind speed) and vector (wind direction) fields strongly affirm the capability of YRD1km to resolve sub-regional atmospheric



347 dynamics. These results further highlight the dataset's potential for supporting a broad spectrum  
 348 of regional meteorological applications.



349  
 350 *Figure 4. Spatial distribution of daily mean near-surface wind fields over the YRD region on 1*  
 351 *June 2022. Panels (a) and (c) show daily mean 10-m wind speed (WSPD10m) from the ERA5 and*





YRD1km datasets, respectively, overlaid with AWS station observations (colored dots). Panels (b), (d), (e), and (f) show locally enlarged wind vector fields: (b) ERA5 over Shanghai and its surrounding urban agglomeration; (d) YRD1km over the Shanghai metropolitan area; (e) the mountainous region near Hangzhou; and (f) Lake Taihu. Arrows are color-coded by wind speed magnitude and overlaid on shaded terrain elevation, with darker tones indicating higher altitudes.

#### 4.2 Statistical Analysis of the Long-term Time Series of Surface Wind

To assess the temporal performance of the proposed YRD1km dataset, hourly time series analyses of the U10m and V10m wind components were conducted over the YRD region for June 2022. Figures 5 presents the corresponding evolutions of MAE and NSE for both wind components, comparing the YRD1km product (red lines) with the ERA5 reanalysis (blue lines), based on validation against ground-based observational data.

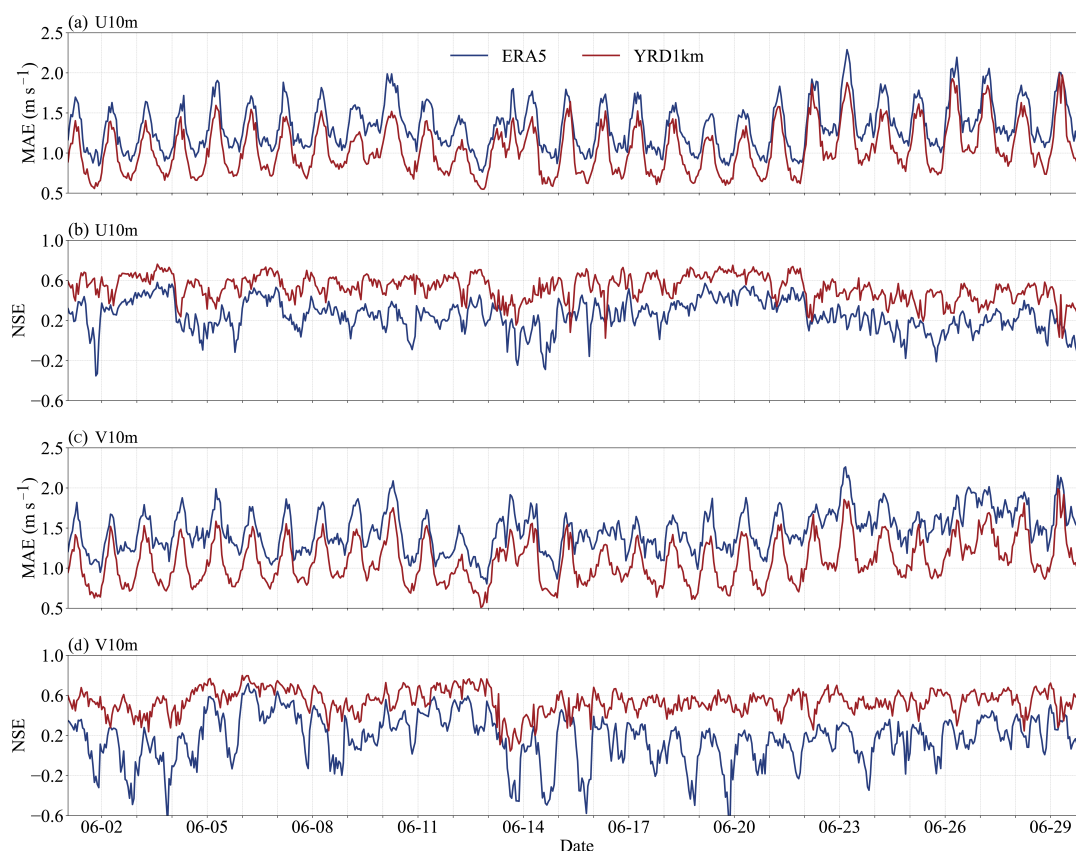
The YRD1km dataset consistently outperforms ERA5 across both components and both metrics. MAE values for YRD1km remain consistently lower than those of ERA5, particularly during nighttime hours, in agreement with the statistical results summarized in Table 4, which show MAE reductions of 21.61% for U10m and 26.04% for V10m. In addition, the RMSE values for U10m and V10m are reduced by 18.30% and 22.63%, respectively. These results indicate the effectiveness of combining multi-source nudging and high-resolution land use data in consistently capturing subtle wind variations over time.

Both wind components exhibit pronounced diurnal cycles in MAE, characterized by peak errors during daytime, particularly around local noon, and reduced errors during nighttime. This pattern reflects the influence of boundary layer dynamics, where daytime convective mixing enhances wind variability and poses greater challenges for model accuracy, whereas nocturnal stability leads to more predictable near-surface wind behavior. The persistence and regularity of





375 this fluctuation across the month highlight the necessity of capturing diurnal processes in high-  
 376 resolution simulations.



377  
 378 *Figure 5. Time series of model performance metrics for hourly 10-m wind components over the*  
 379 *YRD region in June 2022. Panels (a) and (b) show the MAE and NSE, respectively, for the U10m.*  
 380 *Panels (c) and (d) show the corresponding MAE and NSE metrics for the V10m. The red and blue*  
 381 *lines represent the YRD1km and ERA5 datasets, respectively.*

382 In terms of NSE, YRD1km maintains higher and more stable values throughout the month  
 383 for both U10m and V10m. Specifically, NSE values increase by 33.27% for U10m and 40.13% for  
 384 V10m compared to ERA5. While ERA5 frequently exhibits degraded performance, including  
 385 negative NSE values during high-variability periods, YRD1km often sustains NSE above 0.4, with



386 frequent peaks exceeding 0.6, especially during nocturnal hours. This reflects a markedly  
387 improved temporal agreement between modeled and observed wind variations.

388 Overall, the consistent improvements observed across both horizontal wind components  
389 confirm the robustness of the proposed downscaling framework. By effectively addressing both  
390 synoptic-scale and diurnal-scale variability, the YRD1km dataset provides a substantially  
391 enhanced representation of near-surface wind fields in a complex and highly urbanized region such  
392 as the YRD.

393 *Table 4. Evaluation of 10-m wind field simulation performance over the YRD region in June*  
394 *2022.*

| Variable   | Sample size | Indicator | Data  |        | Improvement<br>(%) |
|------------|-------------|-----------|-------|--------|--------------------|
|            |             |           | ERA5  | YRD1km |                    |
| U10m (m/s) | 243280      | MAE       | 1.333 | 1.045  | <b>21.61</b>       |
|            |             | RMSE      | 1.766 | 1.443  | <b>18.30</b>       |
|            |             | NSE       | 0.468 | 0.645  | <b>33.27</b>       |
| V10m (m/s) | 243280      | MAE       | 1.474 | 1.090  | <b>26.04</b>       |
|            |             | RMSE      | 1.938 | 1.500  | <b>22.63</b>       |
|            |             | NSE       | 0.407 | 0.645  | <b>40.13</b>       |

395 **4.3 Evaluation of Vertical Wind Profile Accuracy Using Radiosonde Observations**

396 To comprehensively evaluate the vertical simulation performance of the YRD1km dataset,  
397 radiosonde observations from the Baoshan station in Shanghai were used for the month of June  
398 2022 at 00 and 12 UTC. A comparative analysis was conducted between YRD1km and ERA5  
399 reanalysis data for wind speed accuracy within the 1000–100 hPa pressure range, focusing on both  
400 Bias and RMSE metrics. The YRD1km dataset provides outputs at 32 standard vertical levels,  
401 ranging from 1000 hPa near the surface to 10 hPa in the upper atmosphere. Key pressure levels



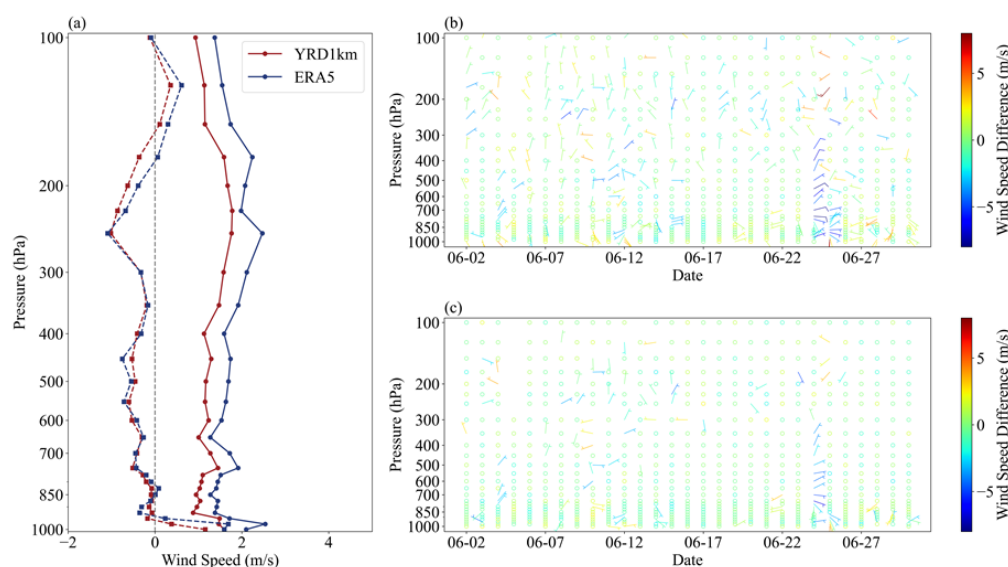
include: 1000, 975, 950, 925, 900, 875, 850, 825, 800, 775, 750, 700, 650, 600, 550, 500, 450, 400, 350, 300, 250, 225, 200, 175, 150, 125, 100, 70, 50, 30, 20, and 10 hPa.

As illustrated in Figure 6a, the vertical profiles of bias (dashed lines) and RMSE (solid lines) reveal that the YRD1km dataset outperforms ERA5 across nearly all pressure levels. The improvements are pronounced in the lower troposphere, benefiting from the dynamic constraints of multi-source observational nudging on near-surface winds and the refined land surface flux representation driven by high-resolution land use data. The maximum reduction in RMSE reaches up to 1.1 m/s at 975 hPa, representing a 42.2% improvement and highlighting the substantial enhancement in near-surface wind speed accuracy provided by YRD1km.

Time–height cross-section of wind vector differences plot (Figures 6b and 6c) further highlights the clear performance of YRD1km. In Figure 6b, ERA5 exhibits frequent and large wind speed differences, often exceeding  $\pm 5$  m/s, along with abrupt directional shifts, particularly within the near-surface layer. Notably, at 00 UTC on June 24, radiosonde data indicate a sharp wind speed increase above the 950 hPa level, exceeding 19.5 m/s, which ERA5 significantly underestimates. This result is consistent with previous studies that have identified ERA5’s limitations in capturing extreme wind events due to its coarser resolution and less-constrained boundary layer parameterizations (Alkhalidi et al., 2025). In contrast, the YRD1km dataset exhibits a more stable vertical wind structure, with smaller deviations from observed values. Although slight underestimations remain during high wind episodes, the magnitude of extreme discrepancies is considerably reduced compared to ERA5. This improvement underscores the effectiveness of the multi-source observational nudging system in locally constraining vertical wind profiles and enhancing model fidelity.



424 In summary, the YRD1km dataset, developed through the synergistic integration of high-  
 425 resolution land surface information and multi-source data assimilation techniques, significantly  
 426 improves not only near-surface wind simulations but also the representation of vertical wind  
 427 structures. This provides a reliable, high-quality data foundation for a wide range of 3D wind field-  
 428 dependent applications, such as low-level wind shear, wind turbine load estimation, pollutant  
 429 cross-layer transport modeling, and urban atmospheric environment studies.



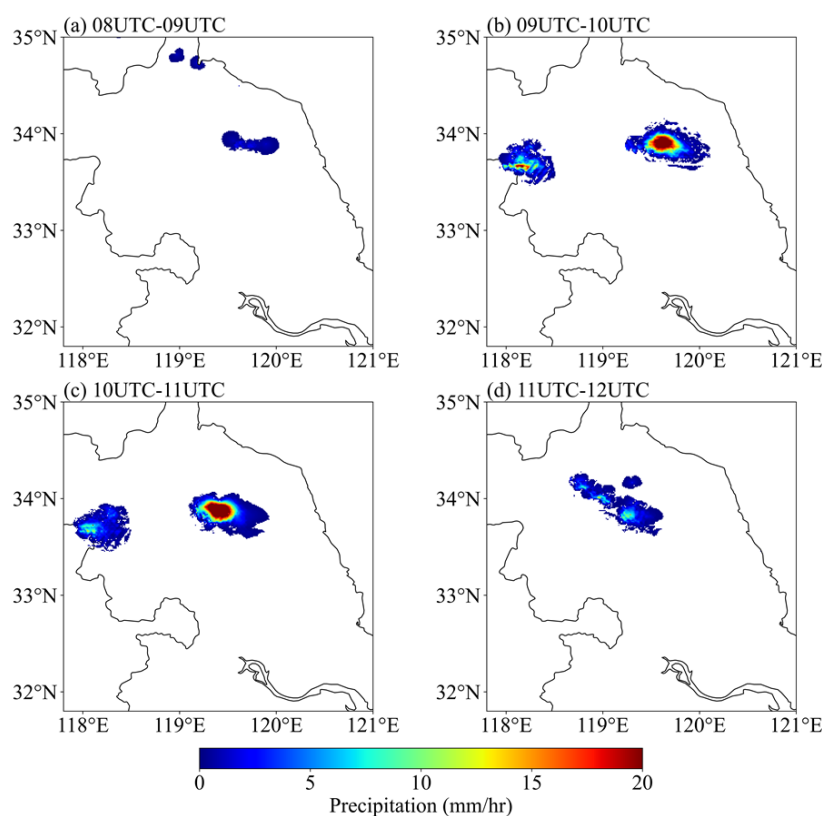
430  
 431 *Figure 6. Vertical evaluation of wind field performance from the YRD1km and ERA5 datasets*  
 432 *against radiosonde observations at the Baoshan station in Shanghai during June 2022. (a) Vertical*  
 433 *profiles of wind speed bias (dashed lines) and RMSE (solid lines) for YRD1km (red) and ERA5*  
 434 *(blue), calculated from all available soundings at 00 and 12 UTC. (b) Time–height cross-section*  
 435 *of wind vector differences between ERA5 and radiosonde observations (RAOB), with wind speed*  
 436 *differences (m/s) indicated by color shading. (c) As in (b), but for YRD1km minus RAOB. Wind*  
 437 *difference plots are shown at 24-hour intervals, beginning at 00 UTC on 2 June 2022.*

#### 438 4.4 Case Study of a Local Severe Convection Event



439 While previous statistical validations have demonstrated the superior performance of the  
 440 YRD1km dataset spatially and temporally, its advantages become even more pronounced in short-  
 441 term, high-impact weather events. In such cases, the dataset's high spatial and temporal resolution  
 442 enhances both early warning capabilities and diagnostic accuracy.

443 As illustrated in Figure 7, a convective storm outbreak occurred over northern Yancheng,  
 444 Jiangsu Province, on the afternoon of 16 June 2022. The event was characterized by highly  
 445 localized and intense precipitation, with peak hourly rainfall rates reaching up to  $20 \text{ mm} \cdot \text{h}^{-1}$ .



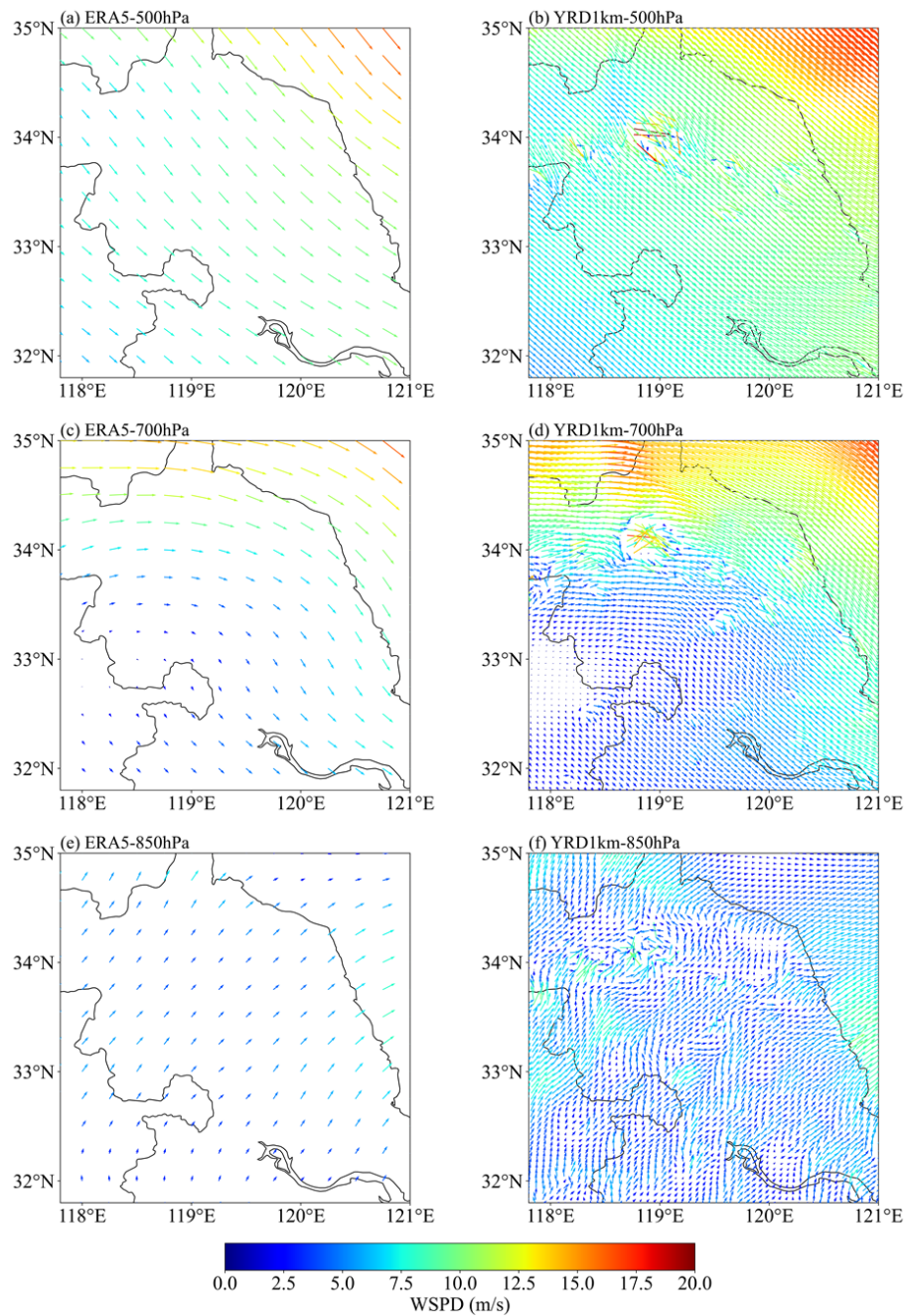
446  
 447 *Figure 7. Hourly evolution of precipitation associated with a convective storm over northern*  
 448 *Yancheng, Jiangsu Province, on 16 June 2022.*



449 To investigate the applicability of the YRD1km dataset in high-impact weather scenarios, this  
450 study conducts a comparative analysis of wind field structures between ERA5 and YRD1km  
451 during the convective event, focusing on three key pressure levels: 500 hPa, 700 hPa, and 850 hPa  
452 (Figure 8). These levels are critical for identifying shear lines, low-level jets, and convective  
453 initiation mechanisms.

454 Overall, the wind field structure in ERA5 appears relatively homogeneous, limiting its ability  
455 to capture mesoscale and sub-mesoscale disturbances. In contrast, YRD1km reveals more detailed  
456 local structures and dynamic features, demonstrating a stronger capacity to resolve mesoscale  
457 systems. Across all three pressure levels, YRD1km consistently captures regions of enhanced wind  
458 speed, wind shear, and convergence. Notably, near 34°N, 119°E at 500 hPa, YRD1km identifies a  
459 localized wind speed maximum exceeding 17.5 m/s and a well-defined shear zone. At 700 hPa, a  
460 clear convergence band and wind speed enhancement area are observed, which is conducive to the  
461 maintenance and development of the convective system. Although wind speeds weaken at 850 hPa,  
462 perturbation signatures remain evident. These structural features spatially align with the center of  
463 heavy precipitation during the event, indicating that YRD1km has enhanced diagnostic capability  
464 in capturing the dynamical background for the initiation and maintenance of deep convective  
465 systems.

466 In summary, the high spatial resolution of YRD1km allows for a more accurate depiction of  
467 wind field structures during severe convective events, thereby improving the diagnosis of key  
468 dynamic mechanisms. This capability contributes to more effective early warning and response  
469 strategies for short-term, high-impact weather events.



470

471 *Figure 8. Comparative analysis of wind field structures between the YRD1km and ERA5 datasets*

472 *during the short-duration severe convective event over Yancheng, Jiangsu Province. Displayed are*





473 *horizontal wind vectors (arrows) and wind speed (color shading) at the (a, b) 500 hPa, (c, d) 700*  
474 *hPa, and (e, f) 850 hPa levels from ERA5 (left column) and YRD1km (right column) at 08:00 UTC*  
475 *on 16 June 2022. For visual clarity, YRD1km wind vectors have been thinned by a factor of three.*

## 476 **5. Conclusions**

477 This study developed and rigorously validated YRD1km, a high-resolution (1 km, hourly)  
478 3D wind field dataset over the YRD region. The dataset was generated through dynamical  
479 downscaling of ERA5 reanalysis data using a customized WRF model configuration. It was further  
480 refined by integrating multi-source observational nudging and updated land use representations to  
481 improve surface parameterization.

482 Comprehensive validations using surface station and radiosonde observations confirmed that  
483 YRD1km significantly outperforms ERA5 in both near-surface and vertical wind simulations. For  
484 10-m wind fields, YRD1km consistently achieved smaller errors and higher skill scores across  
485 MAE, RMSE, and NSE, at both hourly and daily scales. The dataset also better characterizes  
486 spatial variability in wind speed, particularly over complex terrain and densely urbanized areas.  
487 Its wind vector fields align well with underlying geographic features, and monthly statistics show  
488 reductions in MAE and RMSE of approximately 20%, with NSE improved by more than 33%. In  
489 the vertical dimension, YRD1km exhibited reduced RMSE across nearly all pressure levels and  
490 produced observation-consistent vertical profiles. A representative severe convective case over  
491 Yancheng demonstrated YRD1km's ability to resolve fine-scale dynamic signatures, including  
492 wind shear, low-level convergence, and enhanced wind zones, supporting improved diagnosis of  
493 convective development mechanisms.

494 These findings highlight the value of high-resolution datasets enhanced by dynamic  
495 observational constraints in capturing both mesoscale and diurnal variability in complex





environments. The YRD1km product offers a robust foundation for enhancing meteorological applications such as wind energy resource assessment, urban atmospheric modeling, and air pollution transport analysis. Importantly, its fine-scale 3D wind structure also holds significant potential for supporting the monitoring and analysis of low-level wind shear, which is critical for the safe development of low-altitude airspace operations and the broader low-altitude economy in urban regions.

In future work, this framework can be applied to generate longer-term high-resolution wind datasets and extended to other regions characterized by complex terrain and heterogeneous land use. Further enhancements may include incorporating satellite-based measurements and higher-frequency ground-based remote sensing data, as well as coupling with machine learning models to improve real-time forecasting and renewable energy optimization.

#### **Data availability**

The YRD1km 3D wind field dataset is available at <https://doi.org/10.57760/sciencedb.23752> (Zhang et al., 2025).

#### **Author contributions**

ZZ: data collection and processing; writing (original draft preparation). YL: conceptualization; supervision; writing (original draft preparation, review, and editing). XM, PX, and JZ: data collection. ZL, MM, DD, BL, and JL: writing (review and editing).

#### **Competing interests**

The contact author has declared that none of the authors has any competing interests.



519

## 520 **Acknowledgments**

521 We gratefully acknowledge the ECNU Multifunctional Platform for Innovation 001 for providing  
 522 high-performance computing resources. We also thank the ECMWF for access to the ERA5  
 523 reanalysis data, the NCEP for the global upper air and surface weather observations, the CMA for  
 524 providing AWS data, and the ESA for the WorldCover 2020 land use data. Finally, we sincerely  
 525 thank the editor and anonymous reviewers for their insightful comments and constructive  
 526 suggestions, which greatly improved the quality of this manuscript.

527

## 528 **Financial support**

529 This research was supported by the Shanghai Science and Technology Program (Grant No.  
 530 25ZR1401099) and the National Natural Science Foundation of China (Grant No. U2142201).

531

## 532 **References**

- 533 Alkhalidi, M., Al-Dabbous, A., Al-Dabbous, S., and Alzaid, D.: Evaluating the Accuracy of the  
 534 ERA5 Model in Predicting Wind Speeds Across Coastal and Offshore Regions, *J. Mar. Sci. Eng.*,  
 535 13, 149, <https://doi.org/10.3390/jmse13010149>, 2025.
- 536 Anderson, J. T., Hardy, E. E., Roach, J. T., and Witmer, R. E.: A land use and land cover  
 537 classification system for use with remote sensor data, Professional Paper, U.S. Geological Survey,  
 538 <https://doi.org/10.3133/pp964>, 1976.
- 539 Bao, J., Feng, J., and Wang, Y.: Dynamical downscaling simulation and future projection of  
 540 precipitation over China, *J. Geophys. Res. Atmospheres*, 120, 8227–8243,  
 541 <https://doi.org/10.1002/2015JD023275>, 2015.
- 542 Boé, J., Terray, L., Habets, F., and Martin, E.: Statistical and dynamical downscaling of the Seine  
 543 basin climate for hydro-meteorological studies, *Int. J. Climatol.*, 27, 1643–1655,  
 544 <https://doi.org/10.1002/joc.1602>, 2007.
- 545 Collier, E. and Mölg, T.: BAYWRF: a high-resolution present-day climatological atmospheric  
 546 dataset for Bavaria, *Earth Syst. Sci. Data*, 12, 3097–3112, <https://doi.org/10.5194/essd-12-3097->  
 547 2020, 2020.



- 548 Daescu, D. N. and Langland, R. H.: Error covariance sensitivity and impact estimation with adjoint  
 549 4D-Var: theoretical aspects and first applications to NAVDAS-AR, *Q. J. R. Meteorol. Soc.*, 139,  
 550 226–241, <https://doi.org/10.1002/qj.1943>, 2013.
- 551 Dayon, G., Boé, J., and Martin, E.: Transferability in the future climate of a statistical downscaling  
 552 method for precipitation in France, *J. Geophys. Res. Atmospheres*, 120, 1023–1043,  
 553 <https://doi.org/10.1002/2014JD022236>, 2015.
- 554 De Bode, M., Hedde, T., Roubin, P., and Durand, P.: A Method to Improve Land Use  
 555 Representation for Weather Simulations Based on High-Resolution Data Sets—Application to  
 556 Corine Land Cover Data in the WRF Model, *Earth Space Sci.*, 10, e2021EA002123,  
 557 <https://doi.org/10.1029/2021EA002123>, 2023.
- 558 Dudhia, J.: Numerical Study of Convection Observed during the Winter Monsoon Experiment  
 559 Using a Mesoscale Two-Dimensional Model, *J. Atmospheric Sci.*, 46, 3077–3107,  
 560 [https://doi.org/10.1175/1520-0469\(1989\)046<3077:NSOCOD>2.0.CO;2](https://doi.org/10.1175/1520-0469(1989)046<3077:NSOCOD>2.0.CO;2), 1989.
- 561 Dujardin, J. and Lehning, M.: Wind-Topo: Downscaling near-surface wind fields to high-  
 562 resolution topography in highly complex terrain with deep learning, *Q. J. R. Meteorol. Soc.*, 148,  
 563 1368–1388, <https://doi.org/10.1002/qj.4265>, 2022.
- 564 Dupuy, F., Durand, P., and Hedde, T.: Downscaling of surface wind forecasts using convolutional  
 565 neural networks, *Nonlinear Process. Geophys.*, 30, 553–570, [https://doi.org/10.5194/npg-30-553-](https://doi.org/10.5194/npg-30-553-2023)  
 566 2023, 2023.
- 567 Fu, D., Liu, Y., Li, H., Liu, S., Li, B., Thapa, S., Yabo, S., Sun, X., Tang, B., Zuo, J., Qi, H., and  
 568 Tian, C.: Evaluating the Impacts of Land Cover and Soil Texture Changes on Simulated Surface  
 569 Wind and Temperature, *Earth Space Sci.*, 7, e2020EA001173,  
 570 <https://doi.org/10.1029/2020EA001173>, 2020.
- 571 Golzio, A., Ferrarese, S., Cassardo, C., Diolaiuti, G. A., and Pelfini, M.: Land-Use Improvements  
 572 in the Weather Research and Forecasting Model over Complex Mountainous Terrain and  
 573 Comparison of Different Grid Sizes, *Bound.-Layer Meteorol.*, 180, 319–351,  
 574 <https://doi.org/10.1007/s10546-021-00617-1>, 2021.
- 575 Gutowski, W. J., Ullrich, P. A., Hall, A., Leung, L. R., O’Brien, T. A., Patricola, C. M., Arritt, R.  
 576 W., Bukovsky, M. S., Calvin, K. V., Feng, Z., Jones, A. D., Kooperman, G. J., Monier, E., Pritchard,  
 577 M. S., Pryor, S. C., Qian, Y., Rhoades, A. M., Roberts, A. F., Sakaguchi, K., Urban, N., and  
 578 Zarzycki, C.: The Ongoing Need for High-Resolution Regional Climate Models: Process  
 579 Understanding and Stakeholder Information, *Bull. Am. Meteorol. Soc.*, 101, E664–E683,  
 580 <https://doi.org/10.1175/bams-d-19-0113.1>, 2020.
- 581 Harkey, M. and Holloway, T.: Constrained dynamical downscaling for assessment of climate  
 582 impacts, *J. Geophys. Res. Atmospheres*, 118, 2136–2148, <https://doi.org/10.1002/jgrd.50223>,  
 583 2013.
- 584 Hersbach, H., Bell, B., Berrisford, P., Hirahara, S., Horányi, A., Muñoz-Sabater, J., Nicolas, J.,  
 585 Peubey, C., Radu, R., Schepers, D., Simmons, A., Soci, C., Abdalla, S., Abellan, X., Balsamo, G.,



- 586 Bechtold, P., Biavati, G., Bidlot, J., Bonavita, M., De Chiara, G., Dahlgren, P., Dee, D.,  
587 Diamantakis, M., Dragani, R., Flemming, J., Forbes, R., Fuentes, M., Geer, A., Haimberger, L.,  
588 Healy, S., Hogan, R. J., Hólm, E., Janisková, M., Keeley, S., Laloyaux, P., Lopez, P., Lupu, C.,  
589 Radnoti, G., de Rosnay, P., Rozum, I., Vamborg, F., Villaume, S., and Thépaut, J.-N.: The ERA5  
590 global reanalysis, *Q. J. R. Meteorol. Soc.*, 146, 1999–2049, <https://doi.org/10.1002/qj.3803>, 2020.
- 591 Höhle, K., Kern, M., Hewson, T., and Westermann, R.: A comparative study of convolutional  
592 neural network models for wind field downscaling, *Meteorol. Appl.*, 27, e1961,  
593 <https://doi.org/10.1002/met.1961>, 2020.
- 594 Hoke, J. E. and Anthes, R. A.: The Initialization of Numerical Models by a Dynamic-Initialization  
595 Technique, *Mon. Weather Rev.*, 104, 1551–1556, [https://doi.org/10.1175/1520-0493\(1976\)104<1551:tionmb>2.0.co;2](https://doi.org/10.1175/1520-0493(1976)104<1551:tionmb>2.0.co;2), 1976.
- 597 Hong, S.-Y., Noh, Y., and Dudhia, J.: A New Vertical Diffusion Package with an Explicit Treatment  
598 of Entrainment Processes, *Mon. Weather Rev.*, 134, 2318–2341,  
599 <https://doi.org/10.1175/mwr3199.1>, 2006.
- 600 Horvath, K., Koracin, D., Vellore, R., Jiang, J., and Belu, R.: Sub-kilometer dynamical  
601 downscaling of near-surface winds in complex terrain using WRF and MM5 mesoscale models, *J.*  
602 *Geophys. Res. Atmospheres*, 117, <https://doi.org/10.1029/2012JD017432>, 2012.
- 603 Hu, W., Scholz, Y., Yeligeti, M., Bremen, L. von, and Deng, Y.: Downscaling ERA5 wind speed  
604 data: a machine learning approach considering topographic influences, *Environ. Res. Lett.*, 18,  
605 094007, <https://doi.org/10.1088/1748-9326/aceb0a>, 2023.
- 606 Jung, C. and Schindler, D.: On the influence of wind speed model resolution on the global technical  
607 wind energy potential, *Renew. Sustain. Energy Rev.*, 156, 112001,  
608 <https://doi.org/10.1016/j.rser.2021.112001>, 2022.
- 609 Kain, J. S.: The Kain–Fritsch Convective Parameterization: An Update, *J. Appl. Meteorol.*, 43,  
610 170–181, [https://doi.org/10.1175/1520-0450\(2004\)043<0170:TKCPAU>2.0.CO;2](https://doi.org/10.1175/1520-0450(2004)043<0170:TKCPAU>2.0.CO;2), 2004.
- 611 Kotlarski, S., Szabó, P., Herrera, S., Rätty, O., Keuler, K., Soares, P. M., Cardoso, R. M., Bosshard,  
612 T., Pagé, C., Boberg, F., Gutiérrez, J. M., Isotta, F. A., Jaczewski, A., Kreienkamp, F., Liniger, M.  
613 A., Lussana, C., and Pianko-Kluczyńska, K.: Observational uncertainty and regional climate  
614 model evaluation: A pan-European perspective, *Int. J. Climatol.*, 39, 3730–3749,  
615 <https://doi.org/10.1002/joc.5249>, 2019.
- 616 Lei, L. and Hacker, J. P.: Nudging, Ensemble, and Nudging Ensembles for Data Assimilation in  
617 the Presence of Model Error, *Mon. Weather Rev.*, 143, 2600–2610, <https://doi.org/10.1175/MWR-D-14-00295.1>, 2015.
- 619 Lian, J., Huang, S., Shao, J., Chen, P., Tang, S., Lu, Y., and Yu, H.: TerraWind: A Deep Learning-  
620 Based Near-Surface Winds Downscaling Model for Complex Terrain Region, *Geophys. Res. Lett.*,  
621 51, e2024GL112124, <https://doi.org/10.1029/2024GL112124>, 2024.



- 622 Liu, J., Shi, C., Ge, L., Tie, R., Chen, X., Zhou, T., Gu, X., and Shen, Z.: Enhanced Wind Field  
623 Spatial Downscaling Method Using UNET Architecture and Dual Cross-Attention Mechanism,  
624 Remote Sens., 16, 1867, <https://doi.org/10.3390/rs16111867>, 2024a.
- 625 Liu, S., Zeman, C., and Schär, C.: Dynamical Downscaling of Climate Simulations in the Tropics,  
626 Geophys. Res. Lett., 51, e2023GL105733, <https://doi.org/10.1029/2023GL105733>, 2024b.
- 627 Liu, Y., Di, D., Li, J., Li, Z., Ma, Z., Zheng, J., Liu, Y.-A., and Zhang, T.: Consistency Assessment  
628 of the Winds in Reanalysis Datasets and the GIRS Product Using Radiosondes, Adv. Atmospheric  
629 Sci., <https://doi.org/10.1007/s00376-025-4138-x>, 2025.
- 630 Lo, J. C., Yang, Z., and Pielke, R. A.: Assessment of three dynamical climate downscaling methods  
631 using the Weather Research and Forecasting (WRF) model, J. Geophys. Res. Atmospheres, 113,  
632 2007JD009216, <https://doi.org/10.1029/2007JD009216>, 2008.
- 633 Mlawer, E. J., Taubman, S. J., Brown, P. D., Iacono, M. J., and Clough, S. A.: Radiative transfer  
634 for inhomogeneous atmospheres: RRTM, a validated correlated-k model for the longwave, J.  
635 Geophys. Res. Atmospheres, 102, 16663–16682, <https://doi.org/10.1029/97JD00237>, 1997.
- 636 Molina, M. O., Gutiérrez, C., and Sánchez, E.: Comparison of ERA5 surface wind speed  
637 climatologies over Europe with observations from the HadISD dataset, Int. J. Climatol., 41, 4864–  
638 4878, <https://doi.org/10.1002/joc.7103>, 2021.
- 639 Nash, J. E. and Sutcliffe, J. V.: River flow forecasting through conceptual models part I — A  
640 discussion of principles, J. Hydrol., 10, 282–290, [https://doi.org/10.1016/0022-1694\(70\)90255-6](https://doi.org/10.1016/0022-1694(70)90255-6),  
641 1970.
- 642 Nashwan, M. S., Shahid, S., and Chung, E.-S.: Development of high-resolution daily gridded  
643 temperature datasets for the central north region of Egypt, Sci. Data, 6, 138,  
644 <https://doi.org/10.1038/s41597-019-0144-0>, 2019.
- 645 Santos-Alamillos, F. J., Pozo-Vázquez, D., Ruiz-Arias, J. A., and Tovar-Pescador, J.: Influence of  
646 land-use misrepresentation on the accuracy of WRF wind estimates: Evaluation of GLCC and  
647 CORINE land-use maps in southern Spain, Atmospheric Res., 157, 17–28,  
648 <https://doi.org/10.1016/j.atmosres.2015.01.006>, 2015.
- 649 Siewert, J. and Kroszczynski, K.: Evaluation of High-Resolution Land Cover Geographical Data  
650 for the WRF Model Simulations, Remote Sens., 15, 2389, <https://doi.org/10.3390/rs15092389>,  
651 2023.
- 652 Skamarock, W. C., Klemp, J. B., Dudhia, J., Gill, D. O., Liu, Z., Berner, J., Wang, W., Powers, J.  
653 G., Duda, M. G., Barker, D. M., and Huang, X.-Y.: A Description of the Advanced Research WRF  
654 Model Version 4, <https://doi.org/10.5065/1DFH-6P97>, 2019.
- 655 Sun, Y., Deng, K., Ren, K., Liu, J., Deng, C., and Jin, Y.: Deep learning in statistical downscaling  
656 for deriving high spatial resolution gridded meteorological data: A systematic review, ISPRS J.  
657 Photogramm. Remote Sens., 208, 14–38, <https://doi.org/10.1016/j.isprsjprs.2023.12.011>, 2024.



- 658 Tang, J., Niu, X., Wang, S., Gao, H., Wang, X., and Wu, J.: Statistical downscaling and dynamical  
659 downscaling of regional climate in China: Present climate evaluations and future climate  
660 projections, *J. Geophys. Res. Atmospheres*, 121, 2110–2129,  
661 <https://doi.org/10.1002/2015JD023977>, 2016.
- 662 Tareghian, R. and Rasmussen, P. F.: Statistical downscaling of precipitation using quantile  
663 regression, *J. Hydrol.*, 487, 122–135, <https://doi.org/10.1016/j.jhydrol.2013.02.029>, 2013.
- 664 Tewari A. M., Chen A. F., Wang A. W., Dudhia A. J., LeMone A. M. A., Mitchell A. K. E., Ek A.  
665 M. B., Gayno A. G., Wegiel A. J. W., Cuenca A. R., and Society S. A. M.: Implementation and  
666 verification of the unified Noah land-surface model in the WRF model, 20th Conference on  
667 Weather Analysis and Forecasting/16th Conference on Numerical Weather Prediction, Seattle, WA:  
668 American Meteorological Society, 2004.
- 669 Thompson, G., Field, P. R., Rasmussen, R. M., and Hall, W. D.: Explicit Forecasts of Winter  
670 Precipitation Using an Improved Bulk Microphysics Scheme. Part II: Implementation of a New  
671 Snow Parameterization, *Mon. Weather Rev.*, 136, 5095–5115,  
672 <https://doi.org/10.1175/2008mwr2387.1>, 2008.
- 673 Viterbo, F., Sperati, S., Vitali, B., D’Amico, F., Cavalleri, F., Bonanno, R., and Lacavalla, M.:  
674 MERIDA HRES: A new high-resolution reanalysis dataset for Italy, *Meteorol. Appl.*, 31, e70011,  
675 <https://doi.org/10.1002/met.70011>, 2024.
- 676 Xu, Z., Han, Y., Tam, C.-Y., Yang, Z.-L., and Fu, C.: Bias-corrected CMIP6 global dataset for  
677 dynamical downscaling of the historical and future climate (1979–2100), *Sci. Data*, 8, 293,  
678 <https://doi.org/10.1038/s41597-021-01079-3>, 2021.
- 679 Yuan, H., Cheng, L., Pan, Y., Tan, Z., Liu, Q., and Jin, Z.: A multi-level parallel approach to  
680 increase the computation efficiency of a global ocean temperature dataset reconstruction, *J.*  
681 *Parallel Distrib. Comput.*, 192, 104938, <https://doi.org/10.1016/j.jpdc.2024.104938>, 2024.
- 682 Zamo, M., Bel, L., Mestre, O., and Stein, J.: Improved Gridded Wind Speed Forecasts by Statistical  
683 Postprocessing of Numerical Models with Block Regression, *Weather Forecast.*, 31, 1929–1945,  
684 <https://doi.org/10.1175/waf-d-16-0052.1>, 2016.
- 685 Zhang, J., Liu, B., Ren, S., Han, W., Ding, Y., and Peng, S.: A 4 km daily gridded meteorological  
686 dataset for China from 2000 to 2020, *Sci. Data*, 11, 1230, [https://doi.org/10.1038/s41597-024-](https://doi.org/10.1038/s41597-024-04029-x)  
687 [04029-x](https://doi.org/10.1038/s41597-024-04029-x), 2024.
- 688 Zhang, L., Xu, Y., Meng, C., Li, X., Liu, H., and Wang, C.: Comparison of Statistical and Dynamic  
689 Downscaling Techniques in Generating High-Resolution Temperatures in China from CMIP5  
690 GCMs, *J. Appl. Meteorol. Climatol.*, 59, 207–235, <https://doi.org/10.1175/jamc-d-19-0048.1>,  
691 2020.
- 692 Zhang, N., Gao, Z., Wang, X., and Chen, Y.: Modeling the impact of urbanization on the local and  
693 regional climate in Yangtze River Delta, China, *Theor. Appl. Climatol.*, 102, 331–342,  
694 <https://doi.org/10.1007/s00704-010-0263-1>, 2010.



695 Zhang, S. and Li, X.: Future projections of offshore wind energy resources in China using CMIP6  
696 simulations and a deep learning-based downscaling method, *Energy*, 217, 119321,  
697 <https://doi.org/10.1016/j.energy.2020.119321>, 2021.

698 Zhang, Z. and Liu, Y.-A.: A 1 km Hourly High-Resolution 3D Wind Field Dataset over the Yangtze  
699 River Delta during June-August 2021-2023, *Science Data Bank* [data set],  
700 <https://doi.org/10.57760/sciencedb.23752>, 2025.

701